Feasibility of transcranial photoacoustic imaging for interventional guidance of endonasal surgeries

Muyinatu A. Lediju Bell,[*a] Anastasia K. Ostrowski,[a,b] Peter Kazanzides,[a] and Emad Boctor[a,c]

[a]Johns Hopkins University, Department of Computer Science, Baltimore, MD, USA
[b]University of Michigan, Department of Biomedical Engineering, Ann Arbor, MI, USA
[c]Johns Hopkins University, Department of Radiology, Baltimore, MD, USA

ABSTRACT

Endonasal surgeries to remove pituitary tumors incur the deadly risk of carotid artery injury due to limitations with real-time visualization of blood vessels surrounded by bone. We propose to use photoacoustic imaging to overcome current limitations. Blood vessels and surrounding bone would be illuminated by an optical fiber attached to the endonasal drill, while a transducer placed on the pterional region outside of the skull acquires images. To investigate feasibility, a plastisol phantom embedded with a spherical metal target was submerged in a water tank. The target was aligned with a 1-mm optical fiber coupled to a 1064nm Nd:YAG laser. An Ultrasonix L14-5W/60 linear transducer, placed approximately 1 cm above the phantom, acquired photoacoustic and ultrasound images of the target in the presence and absence of 2- and 4-mm-thick human adult cadaveric skull specimens. Though visualized at 18 mm depth when no bone was present, the target was not detectable in ultrasound images when the 4-mm thick skull specimen was placed between the transducer and phantom. In contrast, the target was visible in photoacoustic images at depths of 17-18 mm with and without the skull specimen. To mimic a clinical scenario where cranial bone in the nasal cavity reduces optical transmission prior to drill penetration, the 2-mm-thick specimen was placed between the phantom and optical fiber, while the 4-mm specimen remained between the phantom and transducer. In this case, the target was present at depths of 15-17 mm for energies ranging 9-18 mJ. With conventional delay-and-sum beamforming, the photoacoustic signal-to-noise ratios measured 15-18 dB and the contrast measured 5-13 dB. A short-lag spatial coherence beamformer was applied to increase signal contrast by 11-27 dB with similar values for SNR at most laser energies. Results are generally promising for photoacoustic-guided endonasal surgeries.

Keywords: transcranial optoacoustic imaging, pituitary tumors, image-guided surgical navigation, skull base surgery, intraoperative imaging of neurovasculature, endonasal tumor resection

1. INTRODUCTION

Transsphenoidal surgery is the most common method for removal of pituitary tumors.[1] It is a minimally-invasive procedure in which instruments such as a drill for sphenoidal bone removal and a curette for tumor resection are passed through the nostrils and nasal septum to access the sphenoid sinus and resect the tumor. In endoscopic endonasal transsphenoidal surgery, an endoscope is inserted through an incision at the rear of the nasal septum, for visualization of the surgical field. The endoscope is not capable of visualizing vessels hidden behind the sphenoidal bone.

Injury to the carotid arteries, which are located behind the sphenoid on either side of the pea-sized pituitary gland, is a significant complication of transsphenoidal surgery that causes severe blood loss, stroke, or death. It may be treated with emergency interventions, albeit with a high risk of irreversible neurological damage.[2] This complication occurs most frequently with novice surgeons who have performed fewer than 200-500 of these surgeries and thus are not sufficiently familiar with potential variations in the anatomy surrounding the pituitary gland.[3] In addition, this procedure is particularly challenging in pediatric patients who are born with small nasal cavities that mainly develop into their full size after puberty.[4, 5]
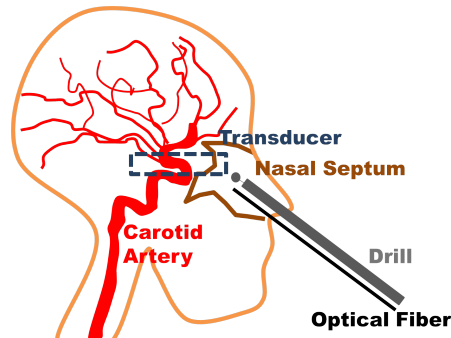
---

*E-mail:muyinatu.ledijubell@jhu.edu

Figure 1. Schematic illustration of the proposed photoacoustic imaging system setup. A transducer is placed on the temporal region on the outside of the patient's skull (and skin), as indicated by the dashed box, while an optical fiber attached to the surgical drill is inserted into the nasal septum.

The availability of imaging methods for localizing blood vessels during endonasal surgery would assist with reducing the occurrence of carotid artery injury. Intraoperative CT may be used for guidance of the bony anatomy surrounding the pituitary tumor,[6] however, it does a poor job of visualizing blood vessels and incurs the risks associated with radiation exposure. Magnetic resonance angiography is another option,[7] but it is costly and patients with pacemakers or metal implants are not suitable candidates for this approach. In addition, these imaging modalities are not quite real-time as one volumetric reconstruction could take as long as 20 minutes. Transcranial ultrasound is a potential option, but it requires low transmit frequencies for skull penetration, which translates to poor spatial resolution and a necessity for expert sonographers to interpret images.[8]

Real-time photoacoustic imaging[9] is a faster, safer, less expensive option which generates images by emitting nanosecond light pulses from a laser.[10] When the light irradiates a target, such as bone or vessels, the target absorbs the light, according to its optical absorption spectrum. Optical absorption causes thermoelastic expansion and generates acoustic waves that are detectable with an ultrasound transducer. Photoacoustic imaging is advantageous over conventional ultrasound imaging because there is less acoustic interaction with the skull. The acoustic waves are only required to pass through the skull one time, rather than twice as in pulse-echo ultrasound and as a result, the waves are less susceptible to the sound scattering and aberrations that occur when they encounter the skull. The feasibility of transcranial photoacoustic imaging was previously demonstrated with neonatal and adult skulls.[11–13]

This paper presents our preliminary investigations into the feasibility of photoacoustic imaging for guiding endonasal surgeries. We envision that a transducer would be placed on the temporal region of the patient's skull, as indicated by the dashed box in Fig. 1. The temporal region includes the pterion bone which is the thinnest portion of the human skull measuring 1-4.4 mm thick.[14] The optical fiber, coupled to a laser, would be attached to a surgical drill. During the surgery, the drill and optical fiber would be inserted into the nasal passage where the optical fiber would illuminate the sphenoid bone (located at the rear of the nasal septum), which has a thickness of approximately 2 mm.[15] Intraoperative photoacoustic images will be acquired to visualize hidden blood vessels as surgeons are drilling to remove the sphenoidal bone.

2. METHODS

2.1 Phantom Experiments

A plastisol phantom embedded with a spherical metal target was submerged in a water tank to investigate the feasibility of target visualization in the presence of acoustic and optical interference from cranial bone. An Ultrasonix L14-5W/60 linear transducer with a bandwidth of 5-14 MHz was placed approximately 1 cm above the phantom to acquire ultrasound and photoacoustic image data. A 1-mm core diameter optical fiber with a 0.37 numerical aperture was coupled to a 1064 nm Nd:YAG laser and the free end of the fiber was placed orthogonal to the probe, as shown in Fig. 2(a). The transducer was connected to a SonixTouch ultrasound scanner, and a SonixDAQ data acquisition unit was triggered by the flashlamp output signal of the laser to access raw, pre-beamformed radiofrequency (RF) photoacoustic data.
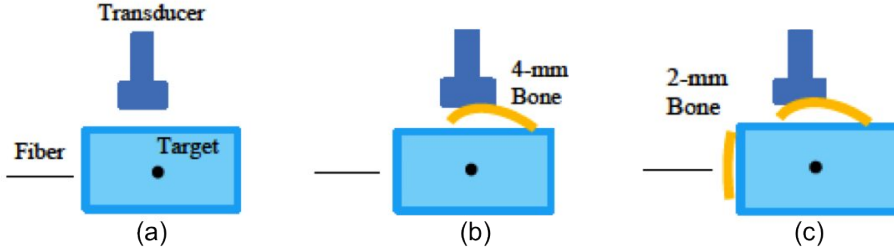
Figure 2. (a) Experimental setup of a spherical metal target embedded in a plastisol phantom in the absence of adult cadaveric skull specimens. (b) A 4-mm thick skull specimen was added between the phantom and transducer. (c) A 2-mm thick skull specimen was added between the fiber and phantom.

A 4-mm thick, formalin-fixed, human adult cadaveric skull specimen was placed between the phantom and ultrasound probe, which represents an imaging scenario after the sphenoidal bone is removed, as illustrated in Fig. 2(b). Pre-beamformed RF photoacoustic data were acquired at an energy of 18mJ with and without this bone in place.

A similar 2-mm thick, formalin-fixed human adult cadaveric skull specimen was then added between the phantom and optical fiber to investigate imaging feasibility prior to drill penetration, as shown in Fig. 2(c). For this experiment, the energy at the tip of the optical fiber was varied from 9 to 18 mJ, and six frames of pre-beamformed RF photoacoustic data were acquired for each laser energy.

2.2 Beamforming of Photoacoustic Data

Conventional beamformers, like delay-and-sum (DAS), use an amplitude-based approach that suffers from poor contrast when the laser fluence and penetration is insufficient. A coherence-based approach, like short-lag spatial coherence (SLSC), has potential to overcome the traditional limitations associated with insufficient laser penetration, because the SLSC beamformer measures and displays the acoustic wavefield's spatial coherence, which is independent of signal amplitude.[16,17] The SLSC beamformer was previously applied to photoacoustic images to improve the contrast of various targets.[16,18]

The DAS and SLSC beamformers were applied to the acquired data by first delaying the signals received by the transducer to account for differences in arrival time, where $s_i(n)$ represents the time-delayed signal received by the ith transducer element at sample number (or depth), n. One pixel in a DAS image was obtained by summation of all s_i at a particular depth n. To apply the SLSC beamformer, the normalized spatial coherence across the receive aperture, $\hat{R}$, and the resulting short-lag spatial coherence, R_{sl}, was calculated as follows:[17,19]

$$\hat{R}(m) \quad = \quad \frac{1}{N-m} \sum_{i=1}^{N-m} \frac{\sum_{n=n_1}^{n_2} s_i(n) s_{i+m}(n)}{\sqrt{\sum_{n=n_1}^{n_2} s_i^2(n) \sum_{n=n_1}^{n_2} s_{i+m}^2(n)}}, \tag{1}$$

$$R_{sl} \quad = \quad \sum_{m=1}^{M} \hat{R}(m), \tag{2}$$

where m is the lateral spacing, or lag, between two elements on the receive aperture, N is the number of receive elements, and M is the maximum number of lags integrated to make an SLSC image. One pixel in a SLSC photoacoustic image is formed by computing Eqs. 1 and 2 at a depth n of the channel signals, using a correlation kernel size equal to $n_2 - n_1$, centered about n.

The performance of the two beamformers was evaluated by measuring target contrast and signal-to-noise ratios (SNR) as follows:

$$\text{Contrast} \quad = \quad 20\log_{10}\left(\frac{S_i}{S_o}\right) \tag{3}$$

$$\text{SNR} \quad = \quad 20\log_{10}\left(\frac{S_i}{\sigma_o}\right) \tag{4}$$
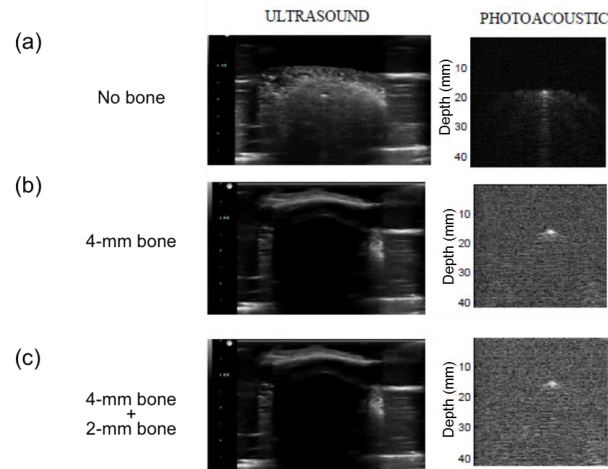
Figure 3. Ultrasound and photoacoustic images of spherical metal target embedded in a plastisol phantom in the (a) absence and presence of (b) the 4-mm thick skull specimen and (c) both the 4-mm and 2-mm thick skull specimens. Results indicate that it is possible to detect a target in the presence of human adult skull specimens with photoacoustic imaging in cases where ultrasound imaging fails.

where S_i and S_o are the means of the image data within regions of interest (ROIs) located inside and outside of the target, respectively, and σ_o is the standard deviation of the data within the ROI located outside of the target. ROIs surrounding the maximum signal from the target were manually selected, and a matching ROI at the same depth and with the same size was automatically created.

3. RESULTS

Ultrasound and photoacoustic images of the metal target in the absence and presence of the skull specimens are shown in Fig. 3. When no bone was present (Fig. 3(a)), the phantom and target were clearly visualized in the ultrasound image, while only the target is visible in the photoacoustic image. The presence of the 4-mm bone placed between the phantom and transducer (Fig. 3(b)) inhibited ultrasound imaging of the target within the 5-14 MHz bandwidth of the probe. However, the target was still visualized in the photoacoustic image, albeit with lower SNR. The target was similarly visualized when the skull specimen was added between the fiber and phantom (Fig. 3(c)). The photoacoustic images shown in Fig. 3 were created with DAS beamforming.

SLSC beamforming was implemented to compare with DAS beamforming results. Coherence curves were calculated using Eq. 1. In general, the targets have higher spatial coherence across the receiver compared to the noise regions surrounding them. Fig. 4(a) shows the coherence curves of the target and noise regions when both skull specimens were present (as depicted in Fig. 2(c)). In the absence of the skull specimens, signals from the target had higher spatial correlation than that shown in Fig. 4, indicating that the presence of cranial bone reduces the spatial coherence of acoustic waves emanating from a target.

Coherence curves like those shown in Fig. 4(a) were integrated, as described by Eq. 2, to create the SLSC images shown in Fig. 4 (b), acquired at the laser energy indicated above each image. The integral of the noise region is lower than that of the target, particularly in the short-lag region (e.g. the region where receive element spacings range from 1 to 10).

Image improvements were achieved with the SLSC beamformer, compared to the DAS beamformer, as shown in Fig. 5. The mean contrast of the target in the SLSC beamformed images was 11-27 dB greater than that in matched DAS beamformed images, as measured from five image acquisitions at each energy level. However, at lower energies (e.g. 9 mJ), although contrast was improved, the mean SNR in SLSC images was reduced by up to 3 dB, compared to that of the DAS images.
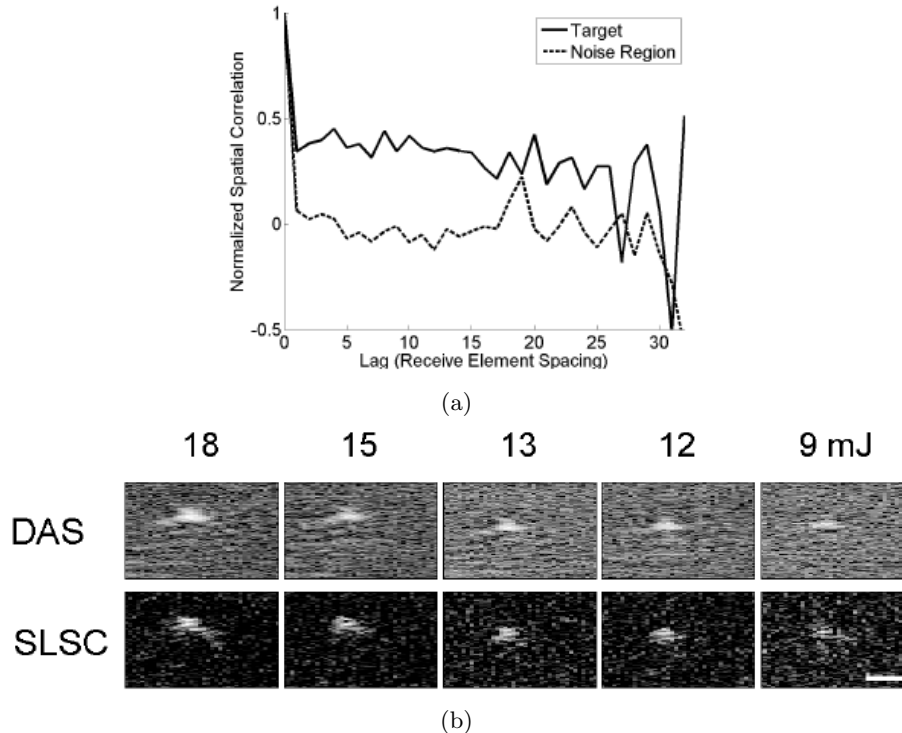
(a)

(b)

Figure 4. (a) Example of coherence curves used to form SLSC photoacoustic images. (b) Delay-and-sum (DAS) vs. SLSC beamforming as energy at the tip of the fiber is varied. The white line, 5mm in length, indicates the image scale. All images are all shown with 25 dB dynamic range.
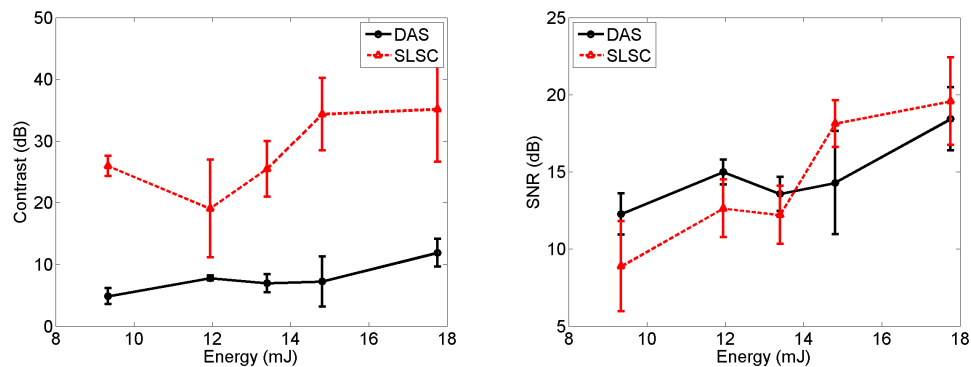

Figure 5. (a) Contrast and (b) SNR in the DAS and SLSC photoacoustic images as a function of energy. Results are reported as the mean ± one standard deviation of the six images acquired at each energy level.

4. DISCUSSION

Preliminary work with a spherical metal target embedded in a plastisol phantom indicates that it is possible to detect a target in the presence of human adult skull specimens, as shown in Fig. 3. The target was located at a depth of 18 mm with no bone and 17 mm when the 4-mm thick bone was placed between the transducer and the phantom, which is consistent with the expected depth shift due to sound speed inhomogeneities between the bone and the phantom. Thus, a transcranial photoacoustic image will not depict the true depth of vessels if sound speed differences are not taken into account during image reconstruction, as noted by Jin *et al.*[20] One implication for clinical translation is that a margin of error that corresponds with the expected depth shifts should be added to the visualized vessels if no sound speed corrections are applied prior to image display.

The sound aberrations caused by cranial bone reduces the SNR of received photoacoustic signals. Thus,

beamforming plays a critical role in the image quality that can be achieved with transcranial photoacoustic imaging. Application of a coherence-based SLSC beamformer improved signal contrast by up to 27 dB, compared to the conventional amplitude-based DAS beamformer. Similar advanced beamformers should be investigated in more detail to achieve optimal image quality for the proposed application.

One limitation of the presented study is that the imaging target was a metal sphere, which has significantly different optical absorption and scattering properties compared to blood. Nonetheless, the goal of the feasibility study was achieved, and results indicate that it is possible to detect a photoacoustic target in the presence of acoustic and optical interference from cranial bone. Future work will include investigations with targets that are more similar to the carotid artery.

5. CONCLUSION

The feasibility of transcranial photoacoustic imaging for guiding endonasal surgery was investigated with favorable results. Namely, the presence of skull bone did not impede target visualization with photoacoustic imaging, as it did in ultrasound imaging. Although image contrast was reduced when skull specimens were placed between the phantom and the transducer, results indicate that advanced beamformers have potential to overcome this limitation. Particularly, the coherence-based SLSC beamformer improved image contrast by up to 27 dB. These results are generally promising for real-time photoacoustic image guidance during endonasal surgeries.

ACKNOWLEDGMENTS

REFERENCES

[1] Debraj Mukherjee, Hasan A Zaidi, Thomas Kosztowski, Kaisorn L Chaichana, Roberto Salvatori, David C Chang, and Alfredo Quiñones-Hinojosa. Predictors of access to pituitary tumor resection in the United States, 1988–2005. *European Journal of Endocrinology*, 161(2):259–265, 2009.

[2] O Reich, K Ringel, P Stoeter, and J Maurer. Injury of ICA during endonasal sinus surgery and management by endovascular stent application. *Laryngorhinootologie*, 88(5):322–326, 2009.

[3] Ivan Ciric, Ann Ragin, Craig Baumgartner, and Debi Pierce. Complications of transsphenoidal surgery: results of a national survey, review of the literature, and personal experience. *Neurosurgery*, 40(2):225–237, 1997.

[4] James L. Frazier, Kaisorn Chaichana, George I. Jallo, and Alfredo Quinones-Hinojosa. Combined endoscopic and microscopic management of pediatric pituitary tumors through one nostril: technical note with case illustrations. *Childs Nervous Systems*, 24(12):1469–1478, 2008.

[5] Sam Jacob. *Human Anatomy: A Clinically-orientated Approach: an Illustrated Colour Text*. Elsevier Health Sciences, 2007.

[6] K Kitazawa, H Okudera, T Takemae, and S Kobayashi. CT guided transsphenoidal surgery: report of nine cases. *No shinkei geka. Neurological surgery*, 21(2):147, 1993.

[7] Rudolf Fahlbusch, Oliver Ganslandt, Michael Buchfelder, Werner Schott, and Christopher Nimsky. Intraoperative magnetic resonance imaging during transsphenoidal surgery. *Journal of neurosurgery*, 95(3):381–390, 2001.

[8] Oleg Y Chernyshev, Zsolt Garami, Sergio Calleja, Joon Song, Morgan S Campbell, Elizabeth A Noser, Hashem Shaltoni, Chin-I Chen, Yasuyuki Iguchi, James C Grotta, et al. Yield and accuracy of urgent combined carotid/transcranial ultrasound testing in acute cerebral ischemia. *Stroke*, 36(1):32–37, 2005.

[9] Nathanael Kuo, Hyun Jae Kang, Danny Y Song, Jin U Kang, and Emad M Boctor. Real-time photoacoustic imaging of prostate brachytherapy seeds using a clinical ultrasound system. *Journal of biomedical optics*, 17(6):0660051–0660057, 2012.

[10] Minghua Xu and Lihong V Wang. Photoacoustic imaging in biomedicine. *Review of scientific instruments*, 77(4):041101–041101, 2006.

[11] Xueding Wang, David L. Chamberland, and Xi Guohua. Noninvasive reflection mode photoacoustic imaging through infant skull toward imaging of neonatal brains. *Journal of Neuroscience Methods*, 168:412–421, 2007.

[12] Xueding Wang, J Brian Fowlkes, David L Chamberland, Guohua Xi, and Paul L Carson. Reflection mode photoacoustic imaging through infant skull toward noninvasive imaging of neonatal brains. In *SPIE BiOS: Biomedical Optics*, pages 717709–717709. International Society for Optics and Photonics, 2009.

[13] Liming Nie, Xin Cai, Konstantin Maslov, Alejandro Garcia-Uribe, Mark A. Anastasio, and Lihong V. Wang. Photoacoustic tomography through a whole adult human skull with a photon recycler. *Journal of Biomedical Optics*, 17(11):110506, 2012.

[14] Siyan Ma, Louisa Baillie, J. M., and Mark D. Stringer. Reappraising the surface anatomy of the pterion and its relationship to the middle meningeal artery. *Clinical Anatomy*, 25(3):330–339, 2012.

[15] Hosemann, W. and Gross, R. and Göde, U. and Kühnel, T. and Röckelein, G. The anterior sphenoid wall: relative anatomy for sphenoidotomy. *American Journal of Rhinology*, 9(3):137–144, 1995.

[16] Muyinatu A. Lediju Bell, Nathanael Kuo, Danny Y. Song, and Emad M. Boctor. Short-lag spatial coherence beamforming of photoacoustic images for enhanced visualization of prostate brachytherapy seeds. *Biomedical Optics Express*, 4(10):1964–1977, 2013.

[17] Muyinatu A. Lediju, Gregg E. Trahey, Brett C. Byram, and Jeremy J. Dahl. Short-lag spatial coherence of backscattered echoes: Imaging characteristics. 58(7):1337, 2011.

[18] Behnaz Pourebrahimi, Sangpil Yoon, Dustin Dopsa, and Michael C Kolios. Improving the quality of photoacoustic images using the short-lag spatial coherence imaging technique. In *SPIE BiOS*, pages 85813Y–85813Y. International Society for Optics and Photonics, 2013.

[19] R. J. Fedewa, K. D. Wallace, M. R. Holland, J. R. Jago, G. C. Ng, M. R. Rielly, B. S. Robinson, and J. G. Miller. Spatial coherence of the nonlinearly generated second harmonic portion of backscatter for a clinical imaging system. 50(8):1010–1022, 2003.

[20] Xing Jin, Changhui Li, and Lihong V Wang. Effects of acoustic heterogeneities on transcranial brain imaging with microwave-induced thermoacoustic tomography. *Medical physics*, 35:3205, 2008.